Approaching the Limits of Aspect Ratio in Free-Standing Al$_2$O$_3$ 3D Shell Structures

Stephanie Burgmann, Markus Lid, Settasit Chaikasetsin, Dag Skjerven Bjordal, Fritz Prinz, John Provine, Filippo Berto, Antonius T. J. van Helvoort, and Jan Torgersen*

Nanoscale free-standing membranes are used for a variety of sensors and other micro/nano-electro-mechanical systems devices. To tune performance, it is indispensable to understand the limits of aspect ratios achievable. Herein, vapor hydrofluoric (VHF) processes are employed to release 3D shell structures made of atomic-layer-deposited Al$_2$O$_3$ etch-stop layers. Structure heights of 100–600 nm and widths of 1–200 nm are fabricated for membranes with 20 and 50 nm thickness. Undercut depths of 500 μm and aspect ratios of 475:1 etch depth to structure width (50 nm films) and etch depth to membrane thicknesses of 495:0.02 (20 nm films) are achieved. The etch-rate stagnates above a ratio of 31% hydrofluoric (HF), where decreasing EtOH shares reduce reproducibility. Etch rates reach 0.75 mm min^{-1} and are generally constant over vapor etch depth. For 100 nm heights and widths of 2 μm, etch rates however stagnate for deeper depths. All explored structures remained stable with widths up to 5 μm independent of the height. Above 10 μm width, top membranes deflect, likely from stress accumulated during deposition. Herein, exploring and understanding the limits of aspect ratio in future free-standing membrane devices are helped.

1. Introduction

Membrane-based microstructures have a wide field of application, including the use of thin film windows for characterization experiments.[1] For example, in situ transmission electron microscope (TEM) analysis of gas-phase reactions could profit from gas-tight cavities integrated into a single silicon chip rather than relying on sealing rings or bonding to seal gas between two chips.[2–5] This reduces potential leaks and saves volume but requires large-area gas-tight cavities that may have the form of free-standing membrane shell structures.[6] In this regard, vapor etch processes and thin, high-quality etch-stop layers set the current standard in achievable aspect ratios as this process is not susceptible to detrimental capillary effects.[7–9] For example, complementary metal-oxide-semiconductor devices profit from obtainable precision in vapor release processes to reproducible free electrical connections.[10] Recent studies utilized atomic-layer-deposited (ALD) ultrathin films as high-quality etch-stop layers with obtainable selectivities of 4000:1 SiO$_2$:Al$_2$O$_3$ using vapor hydrofluoric (VHF) or vapor xenon difluoride (XeF$_2$).[11–13] This shows that the combination of vapor-phase release processes and thinnest etch-resistant films of just a few nanometer thickness deposited by ALD enables remarkable overhangs in free-standing membrane structures.[14,15] However, control over these processes becomes increasingly important and difficult as films get thinner and aspect ratios get higher. For example, thick ALD Al$_2$O$_3$ etch-stop layers sandwiched between two plasma-enhanced chemical vapor-deposited (PECVD) SiO$_2$ films can get damaged when released with fast etch protocols but remain intact with slow etches.[16] However, this observation was not further reasoned. Conventional approaches to achieve free-standing membranes are mostly limited to backside etching and selective underetching by removing sacrificial material. With the former method (e.g., backside wet etching), aspect ratios of 90 000:1 with film thicknesses of 100 nm could be achieved.[17] This approach is however limited to creating a 2D membrane with a defined film thickness that is residing on a dissimilar material underneath. Mechanical properties can only be tailored to a certain degree that is largely dependent on the bulk material properties of the membrane itself.[18–20] The interface between the membrane and the support material underneath often creates a stress

S. Burgmann, M. Lid, D. S. Bjordal, F. Berto, J. Torgersen
Department of Mechanical and Industrial Engineering
NTNU
Trondheim, Norway
E-mail: jan.torgersen@ntnu.no

S. Chaikasetsin, F. Prinz
Department of Mechanical Engineering
Stanford University
Stanford, CA, USA

A. T. J. van Helvoort
Department of Physics
NTNU
Trondheim, Norway

J. Provine
Aligned Carbon (Santa Clara, CA) and
Department of Electrical Engineering
Stanford University

**ADVANCED
SCIENCE NEWS**

www.advancedsciencenews.com

**ADVANCED
ENGINEERING
MATERIALS**

www.aem-journal.com

concentration issue setting a limit to membrane thinness and eventually requiring workarounds such as multilayer architectures or engineered compressive strain.[21–23] Another approach to reduce mechanical constraints at the interface is to deposit a membrane on a sacrificial material that is subsequently etched with XeF_2 or hydrofluoric (HF) vapor to release the membrane.[24] Reported aspect ratio is 3000:1. Structure height was not reported as it was not relevant for most applications. This approach allows a stronger response of the membrane with respect to the backside etching strategy and has resulted in this manufacturing route being applied for the construction of bolometers or other micro-electro-mechanical systems (MEMS) sensors.[25] Due to the limitations in selectivity of sacrificial to membrane material and to enhance the etch rate, the membrane is conventionally equipped with etch holes to allow for effective etching without damaging the membrane. The reported aspect ratios and large device undercuts are therefore limited to roughly 100 µm etch-hole spacing.[26] Here, we want to focus on free-standing continuous 3D shell structures that are released over wide areas without employing backside etching. Such free-standing shell structures shall comprise one material only and shall stem their properties from their geometry in addition to their material. As analogy, shell structures found in nature,[27] and in various engineering structures,[28,29] have advantages in their intrinsic stability over bulk material. Via geometric design, they can access a wider range of elastic properties, way beyond their bulk material properties. In the nanoscale, to the best of our knowledge, such approaches are limited to bottom-up fabrication, where nanotubes or nanowires are fabricated for their use in supercapacitors or as electron field emitters, which stem their performance from tube geometry.[30–32] Here, however, the geometric design is usually limited to heterogeneous patterns of similar structures with restricted size relations.[33] To create nanoscale free-standing shell structures with vastly varying aspect ratios and exact placement, even on one wafer, we want to present a possible method to achieve such defined structures through conformal deposition, lithography, and vapor etching.

Despite its advantages over established techniques, to the best of our knowledge, the process limits of aspect ratio for complex 3D membrane structures with large-area cavities, etched by HF acid, have not been studied, which this work intends to address. In what follows, we explain the process of fabricating suspended release structures using a combination of vapor HF and Al_2O_3 etch-stop layers manufactured by ALD, we present our results on achievable etch depths and etch rates under different process parameters such as gas composition, cycle time, and number of cycles before we discuss results on structure dimensions and possibilities to create deformation-free large-area cavities on a silicon chip.

2. Results and Discussion

Gas-tight membrane-like shell structures can have applicability in in situ gas-phase characterization processes and likely other micro- or nanofluidic applications, wherever the fabrication on a single wafer is important. To understand the limits of manufacturability of these membranes, particularly with regards to achievable aspect ratio, we need to understand:

1) If ultrathin membranes can be conformally coated on sacrificial supports, and if they remain mechanically stable upon release; 2) the achievable etch rates and their dependency on process parameters and shell structure geometry; 3) the reachable etch limits and their dependency on the vapor access to the etch front and etch depth within the shell structure; 4) the etch selectivity of sacrificial material to etch-stop material and its relation to the etch time.

To address these issues, we constructed a set of rectangular profile structures with constant and defined cross sections according to the scheme displayed in **Figure 1**a. These structures contained sacrificial SiO_2 surrounded by ultrathin Al_2O_3 membranes with thicknesses of 20 and 50 nm. Leveraging on the etch selectivity of ALD Al_2O_3 to PECVD SiO_2 (1:4000[12]) extended release processes where performed. Releasing these structures with VHF etching resulted in hollow profiles consisting of
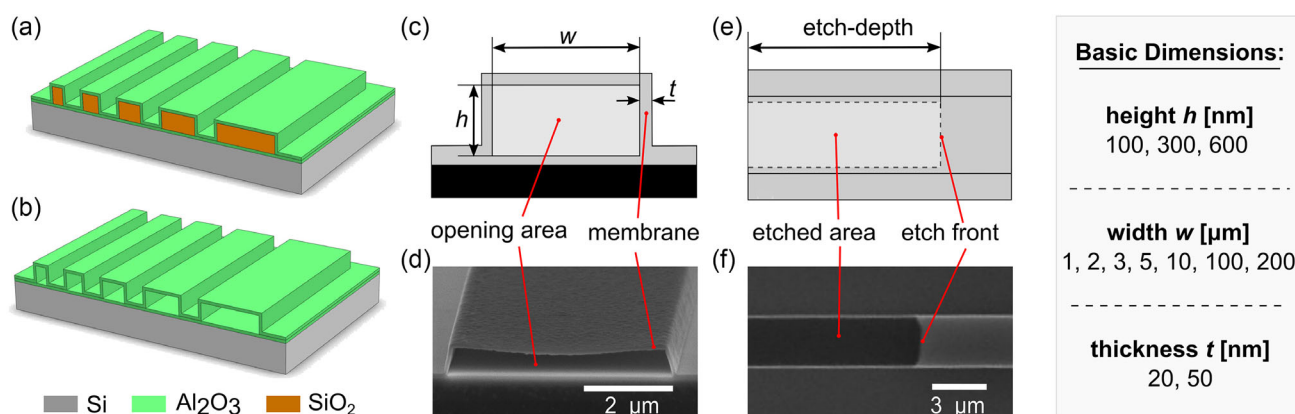

Figure 1. Schematics of the test structure: a) 3D representation of the shell structure with various line widths before the vapor hydrofluoric (VHF) release process. b) The 3D representation of the shell structure after VHF release process. c) Cross-section schematic of the shell structure with basic dimensions of the opening area, and d) Cross-sectional scanning electron microscope (SEM) image of a test structure with 600 nm height, 5 µm width, and 50 nm shell thickness after VHF release process. e) Top-view schematic of a released shell structure with indication of the etch depth. f) Top-view SEM image of the etched shell structure with visible etch front. The basic dimensions are displayed in the figure with the various values chosen for heights, widths, and shell thicknesses.

**ADVANCED
SCIENCE NEWS**

www.advancedsciencenews.com

**ADVANCED
ENGINEERING
MATERIALS**

www.aem-journal.com

Al_2O_3 only thereby forming a set of tunnel-like shell structures, which we refer to as shell structures in the following section (Figure 1b). We are interested in the impact of the vapor etch process parameters (HF content, EtOH content, etch cycle time and total etch time, gas access dimensions) on the etch rate over time and the mechanical stability of the structures. We refer to the key geometrical terms of the shell structures as described in Figure 1. Details of the manufacturing process are provided in Experimental Section.

2.1. Basic Dimensions

To evaluate the limits and possibilities of combining VHF etching and thinnest etch-resistant films deposited in an ALD process, a set of line structures with varying widths, heights, and shell thicknesses was fabricated. Varying the width (w) and height (h) of the shell structures will directly change the size of the opening area, that is, the access area of the etchant to the etch front. We expected the opening area to affect both the dimensional stability and the reachable etch depth of the shell structure, the former due to mechanical limitations and the latter due to concentration and transport limitations of the etchant at and to the etch front. A schematic of the structures released in this study is shown in Figure 1 together with the basic dimensions. The dimensions of the opening area are controlled through the manufacturing process, where the structure height resembles the thickness of the sacrificial material deposited, which, in our case, is the thickness of a PECVD SiO_2 layer shown in Figure 1a. The thickness of the sacrificial layer is defined in the deposition process, where layers with 2% thickness nonuniformity were achieved. The structure width is defined in the lithography process, where the substrate is coated with a photolithographic mask with a 1 μm resolution limit, defining etched and non-etched areas for the subsequent dry etch process. The shell thickness itself is defined in the sub-nanometer regime by the subsequent deposition of the Al_2O_3 ALD layer (conformal coating 3D aspects, 1% thickness nonuniformity). The unique process properties of the ALD process are decisive for the fabrication of nanoscale shell structures. As a result of the etch-resistant and pinhole-free ALD layers surrounding the sacrificial SiO_2 line structures, the VHF etch gas can only progress along the longitudinal tunnel like structures, moving the etch front over time further away from the opening area. Thus, constant etching can only be provided if the supply of etchant to the etch front is faster than or at least equal to the consumption of etchant at the etch front. With increasing undercut length, the exchange of new etchant and byproducts through the longitudinal cavities becomes susceptible to mass transport limitations. Based on this assumption, we can assume that there is a critical opening area where the supply rate of etch gas to the etch front is slower than the consumption rate of etchant at the etch front thus leading to a deceleration or stagnation of the etching process due to conductance issues. The choice of shell structure basic dimensions was inspired by literature. Dry etching processes using XeF_2 structure dimensions with height of 0.5 μm and widths ranging from 1 to 500 μm resulted in undercut depths of around 175 μm within 25 min total etch time.[8] It has to be noted that XeF_2 generates higher initial etch rates than VHF, however, when comparing the

literature studies to our observations with VHF, we observe that etch rates do not decelerate as much over etch depth as reported for XeF_2 processes in literature. This is likely related to the significantly smaller molecular weight of VHF (20.01 g mol^{-1}) compared to XeF_2 (169.29 g mol^{-1}), pointing toward its potentially lower susceptibility to mass transport limitations along its path to the etch front through the longitudinal shell structures. Taking the literature dimensions as a starting point, we hence expected the possibility of releasing deeper overhangs with VHF release processes. Yet, the critical width, height and film thickness can also be mechanical stability limited due to plastic deformation or buckling of the shell membranes. Keeping these assumptions in mind, the structure dimensions were chosen within the resolution limit of the lithography process, where structure widths ranged from 1 to 200 μm. Particularly structures with width ranging from 1 and 10 μm were investigated to address issues of mass transport due to conductance limitations. The structure height was varied ranging from 100 to 600 nm allowing opening areas as small as 0.1 μm^2 and as big as 120 μm^2. The etch selectivity of ALD Al_2O_3 protective layers is impacted by the surrounding materials, the etching time and the process parameters.[16] Fast processes with 150 Torr chamber pressure seem to damage even 100 nm thick ALD Al_2O_3 layers within 1.5 h. However, processes run at 75 Torr chamber pressure with HF_{pp} of 13 Torr show that film thicknesses above 3 nm last for over 1 h in VHF atmosphere. Further, pinhole-type imperfections can cause film damage and, as a result, may lift the film during etching of the underlying substrate. When aiming to evaluate the possibilities of combining VHF and ALD thin films for creating self-supported shell structures with excessive exposure times of up to 11 h, not only the chemical stability of the thin film but also residual stress generated during the etching process has to be taken into account. Stress that accumulates in the film during the deposition processes can cause post-release deformation and rupture of shell structures.[34] This accumulated stress or residual stress in thin films generally changes with growth temperature and film thickness, where thinner films may be less susceptible to deformation than thicker films.[35] Consequently, our hypothesis is that thinner films are less susceptible to deformation but may suffer from insufficient film thickness to resist the etchant over a long etching period. To investigate this hypothesis, two sets of shell structures with selected thicknesses (t) of 20 and 50 nm were studied in this work.

2.2. Conformal Coating and Etch Selectivity

The basic structure dimensions before release can be seen in Figure 1. Even thinnest layers of 20 nm thickness were proven to be stable and self-supporting up to a structure width of 10 μm supporting the previous findings concerning highly effective etch-stop qualities of ALD Al_2O_3.[12] Although measurements with scanning electron microscope (SEM) do not capture the exact entrance dimensions of the shell structure, particularly its thickness, one can argue that the overall dimensions did not significantly change despite etch times of up to 11 h at maximum. We therefore hypothesize that the exposure of the Al_2O_3 etch-stop layers to the etchant is not a process limitation and can be considered negligible when finding optimal process

ADVANCED
SCIENCE NEWS

www.advancedsciencenews.com

ADVANCED
ENGINEERING
MATERIALS

www.aem-journal.com

conditions. However, it has to be noted that in liquid HF etch processes, H_2O is present during oxide etching and increases over prolonged exposures.[36] H_2O can have a detrimental effect on the etch selectivity, as the Al_2O_3 etch-stop layer might get similarly affected in the VHF process. It is therefore important to keep a certain level of EtOH vapor during etching to bind the water to an unreactive byproduct.[37] This has to be considered in the selection of the etch gas composition. It remains to be determined to what extent byproducts can diffuse out of underlying cavities.

2.3. Reproducibility and Etch Rate

The etch selectivity and hence the exposure time of the shell structures to the etchant seem not to be a limitation. It is now to assess what vapor compositions and cycle times give the highest possible etch rates maintaining reproducible processes. For this, we etched a set of predefined shell structures with rectangular profiles using different gas compositions. The vapor compositions of the etch gas and corresponding etch rates are displayed in **Table 1**. The applied vapor compositions and process parameters are designed for typical MEMS processes, where etch rates ranging from 20 to 180 nm min^{-1} can be expected for films formed by thermal oxidation when using recipes R1–R5 with a machine set gas flow limit at ≈ 1900 sccm.[38] The etch rates are however given with reference to the exposed oxide surface. The sample geometry and composition of the etch-stop layer is not considered. In our case, the limited accessibility and a potential etching of Al_2O_3 are expected to influence the etch rates and consequently the achievable aspect ratios and stability of the shell structures. In our case, the amount of available material that may undergo a chemical reaction with VHF is limited to the etch front inside the 3D shell structures. Hence, we expected the etch rate to drastically increase with respect to a full wafer with oxide surface, on which the given etch rates from the manufacturer were measured. Indeed, we observe much higher etch rates than given by the manufacturer, which we attribute to the difference in concentration of HF with respect to the available material for etching. The applied vapor compositions constitute standard recipes provided by the Stanford nanofabrication facility (SNF). Other recipes have to undergo a process qualification.[39,40] The total gas flow was limited to ≈ 1900 sccm according to a recommendation from SPTS, the vendor of the HF vapor equipment. We can show that, by structure design and material choice, etch rates of 40 and
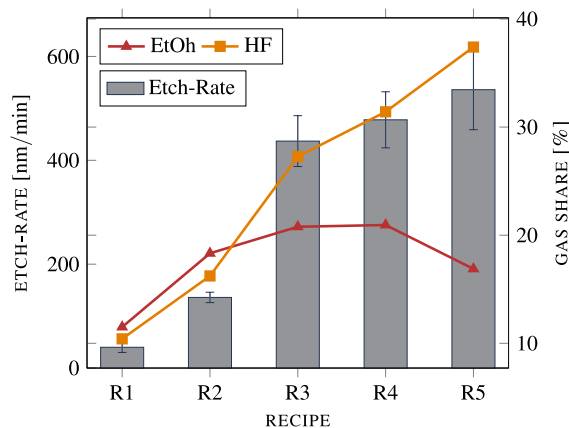

Figure 2. Influence of gas composition on the etch-rate for ten cycle processes. The etch-rate (left axis) displayed in gray with values between 0.04 μm min^{-1} and 0.53 μm min^{-1} includes the standard deviation over all evaluated structures. The gas composition (right axis) displays the gas share for HF and EtOH.

544 nm min^{-1} are reachable for recipes R1–R5 with HF partial pressures (HF_{pp}) ranging from 13 to 46 Torr. However, also the standard deviation increases with increasing HF_{pp} from 10 to 81 nm min^{-1} for recipes R1–R5 for 10 etch cycles, respectively (**Figure 2**). Also, the etch depth increased for a ten cycle process from 1.5 to 21 μm from R1 to R5. To investigate the reproducibility of the etching processes with focus on high etch rates, we included 58 samples in the evaluation of ten cycle processes. Though interesting and useful, the scope of this work was not to benchmark etch recipes but to evaluate the limitations of creating continuous free-standing 3D shell structures with large overhangs. Consequently, to understand the impact of parameters to underetch shell structures in this work, a baseline study was performed which included and investigation of the etch rates for all recipes (R1–R5) on comparable structures. For the sake of throughput, however, lot sizes for the recipes with slow etch rates such as recipe R1 were limited to three samples while recipes with high etch rates such as R4 and R5 included 15 and 19 samples, respectively. Though respective data is not shown, we assume it unlikely that recipes with small HF compositions will damage the membrane material, even over prolonged periods of exposure time. Whether the concentration is then sufficient to reach the etch front when having large overhangs, cannot be concluded from the available data.

For all investigated processes and gas compositions, membranes of and below 10 μm widths remained dimensionally stable over their entire etch depths. Even structures of 100 μm widths, where the top membrane sagged and rested on the underlying support, could be released from the sacrificial SiO_2 indicating that the access to the etch front for facilitating continuous etching was sufficient for all investigated structures. For ten cycles of etching at the given process parameters in Table 1, all available recipes can be chosen, in principle. The choice can fall on the recipe giving high etch rates at limited standard deviations.

Interestingly, there seems to be a significant increase in the HF etch rate between recipes R2 and R3, where subsequent

Table 1. Applied gas compositions for release etch process with ratios of N_2, EtOH, and HF, together with the total gas flow, HF share, and etch rate for a ten cycle process.

Recipe	N_2 [sccm]	EtOH [sccm]	HF [sccm]	Total gas flow [sccm]	HF share [%]	HFpp [torr]	Etch rate [min^{-1}]
R1	1425	210	190	1825	10,41	13,1	40
R2	1250	350	310	1910	16,23	20,28	136
R3	1000	400	525	1925	27,41	34,09	437
R4	910	400	600	1910	31,41	39,2	478
R5	880	325	720	1925	37,40	46,75	536

increases of HF only slightly impact the etch rate. In terms of HF share, a strong increase in the etch rate is observed up to a VHF proportion of 27%. Between R2 and R3 as well as between R3 and R5, the HF share increases by 10%. However, the etch rate more than doubles between R3 and R4, whereas it increases only by around 13% (corresponding to an increase of 327 and 63 nm min^{-1} for R2 to R3 and R3 to R5, respectively). The etch rate seems to saturate with further increases of HF.

Regarding the reproducibility of etch depths, one can see an increase of standard deviations of 0.01 nm min^{-1} between R3 and R4 as well as 0.05 nm min^{-1} between R4 and R5. Since R4 has a significantly higher etch rate with respect to the slight increase in HF content with respect to R3, this recipe was chosen for further investigations. It constitutes a good trade-off between etch speed and reproducibility. This might be related to the decreasing EtOH content in the etchant mixture rendering results less reproducible as the water content catalyzing the reaction may vary over time. The choice of R4 was also substantiated at even longer etch times, where R4 provided superior results in terms of reproducibility over R5 (**Figure 3**). While etch gas enters the etch front through the longitudinal tunnel-like structures, water escaping via alcohol desorption is hampered, which could lead to run-away etches in processes with higher HF content. However, with only slight increases in etch rate with increasing HF share in the etchant, we may argue that the etching process may not be reaction limited. There could be a scenario, where the etchant does not reach the etch front through the entire etch depth due to a transport limitation. This can be explored by investigating the etch rate when etch depths increase and cycle times (the duration of exposure to the HF vapor during one cycles) vary.

To illustrate the effect of the cycle number to the R4 etch rate, etch results for one representative structure are presented in **Figure 4** with respect to exposure time during one cycle (240 and 400 s, respectively). A total of 39 experiments were performed in this study as shown in Figure S8, Supporting Information. Interestingly, the orientation of the shell structure openings in the vapor etch tool also appears to affect the etch rate.
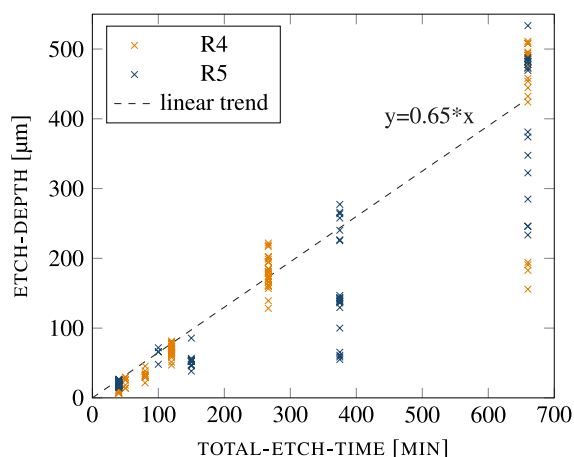

Figure 4. Influence of etch-cycle-time on the etch-rate using gas composition R4. Etching was done on a test structure with varying opening area using etch-cycle-times of 240 and 400 s.

The standard deviation was evaluated for ten structures facing toward the inlet of the vapor etch tool and for wait times of 240 and 400 s, which resulted in a deviation of ±0.04 and ±0.03 mm min^{-1}, respectively. The graph also displays the impact of the opening area (1.2, 3, and 6 µm^2). Three observations can be made. One, there seems to be an initial delay of the etch process, as the etch rate increases with cycle number for the same recipe and the same opening area. Furthermore, particularly in the initial cycles, the etch rate seems to be positively correlated with the size of the opening area. Third, it can be seen that the exposure time is correlated with the etch rate as it increases from 0.63 to 0.74 nm min^{-1} when increasing the cycle time from 240 to 400 s for a 6 µm^2 opening area. Interestingly, this etch rate is then also independent from the cycle number. Particularly for higher cycle numbers with 400 s exposure time, the etch depths were up to 500 µm. The initial etch delay and the impact of the opening area in this phase is interesting but requires further experiments. As this work deals with exploring the limits of aspect ratio, we deem this out of scope and we will elaborate on this aspect in a future study.

Considering the cycle time, however, it is important to note that 400 s do not increase the reactant concentration with respect to 240 s but do lead to an increased etch rate. We therefore chose this setting for our future experiments arguing that there is indeed a kinetic limitation that is however not determined by the shell structure length. Initial experiments with increased exposure times beyond 400 s did not lead to increased etch rates (Figure S7, Supporting Information) and were for matters of throughput not chosen for further experiments in this work. However, these results should be verified in the future. To understand the nature of this kinetic limitation, we want to further study the influence of the cross-sectional dimension of the shell structures. Specifically, we want to see whether the opening area is the limiting factor for achieving large etch depth (**Figure 5**). Both the vendor of the HF vapor equipment and the clean-room facility at Stanford (SPTS, SNF[39]) recommend etch holes with distance between 10 and 100 µm mainly to generate faster etches

Figure 3. Comparison of samples etched with gas composition R4 and R5. Samples with opening area of 1:2, 3, 6 and 60 µm^2 were compared for total etch times up to 660 min. A linear dependence of undercut depth vs. total etch time can be seen for both gas compositions. Only for long total etch times a significant deviation of the etch-depth can be seen.
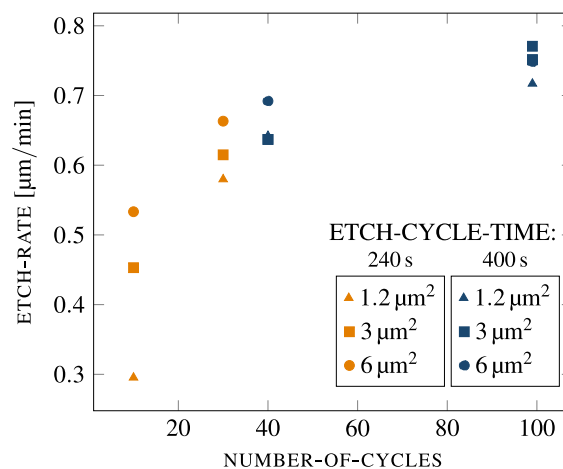
ADVANCED
SCIENCE NEWS
www.advancedsciencenews.com

ADVANCED
ENGINEERING
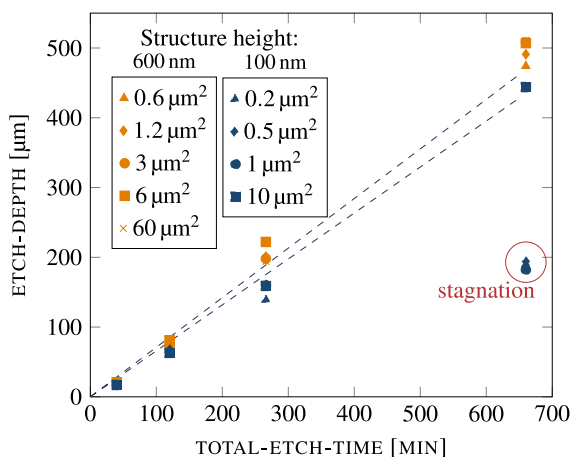MATERIALS
www.aem-journal.com

Figure 5. Influence of structure height and opening area on etch-depth and etch-rate for samples etched with gas composition R4. Etch test were performed on structures with 100 and 600 nm structure height and varying opening area. Regression lines for non stagnating opening areas visualizing the linear etch trend are included for both structure heights.

2.4. Cross-Section Dimension and Etch Depth

Generally, the opening area has an influence on the etch rate and the reachable etch depth, but this influence is small (Figure 5). Up to a total etch time of 266 min, the etch rate has only a very small dependency on the opening area. It is however constant with cycle number (i.e., total etch time) and hence reproducible. There is an impact of the shell structure height, however that determines the linear trend (i.e., the etch rate) only. The average etch rate was 0.7 mm min^{-1} (SD 0.02) and 0.65 mm min^{-1} (SD 0.03) for 600 and 100 nm heights, respectively. This trend continued even beyond 266 min total etch time leading to only slight etch depth deviations. For example, for a structure height of 600 nm and a total etch time of 660 min, the etch depth differs only by 37 μm between an opening area of 0.6 μm^2 (1 μm width) and 60 μm^2 (10 μm width). It has to be noted that the linear trend does not apply to all cross-section dimensions beyond 266 min etch time. The etch rates of structures with height of 100 nm and opening area below 1 μm^2 are stagnating after reaching a total etch depth of 190 μm. The supply of etchant at the etch front in the shell structure is here likely insufficient for the etch process to continue.

As the diffusion seems not to be the limitation (etch rates are constant for larger opening areas), conductance and flow resistance within the shell structure are likely the cause. In this scenario, intermolecular collisions and wall-gas friction may hinder reaching vacuum in the small cavities above a certain etch depth. This may cause a blockage of the cavities and ultimately a stop in etch progression. There could exist a critical etch depth for a corresponding opening area, or vice versa. Here, we want to look into another potential aspect limiting etch progression, and, even more importantly, impacting the proper compliance to the structure's intended function. The mechanical stability of the structure not only ensures fast etch processes with long etch depth, but also determines the deviations to its as-fabricated shape after etching.

2.5. Stability of Membrane Shell Structures

Another reason limiting the access of the etchant to the etch front is the observed sagging of the top membrane toward the silicon substrate as seen in **Figure 6**b,c. To evaluate the extent of deformation, the structure was imaged before etching (Figure 6a,d) and as a focused ion beam (FIB) cut along the underetched structure with a protective platinum (Pt) coating (Figure 6c,d). The phenomenon of sagging occurred particularly on the entire length of wider structures upon a width of 100 and 200 μm. These wide structures completely collapsed (Figure S4e, Supporting Information). However, already at widths of 10 μm, the top membrane severely deformed at the opening area limiting the access of etch gases to the etch front for deeper etches. The deformation primarily happens near the opening area only and subsides as the etch goes deeper into the channel. This deformation can be considered limiting both in terms of reachable etch depths and in terms of aspect ratio. It is therefore important to understand the nature of this deformation and possibly find strategies to circumvent it. Gravity likely has no impact in the nanometer regime. To elaborate this, we employ a thought
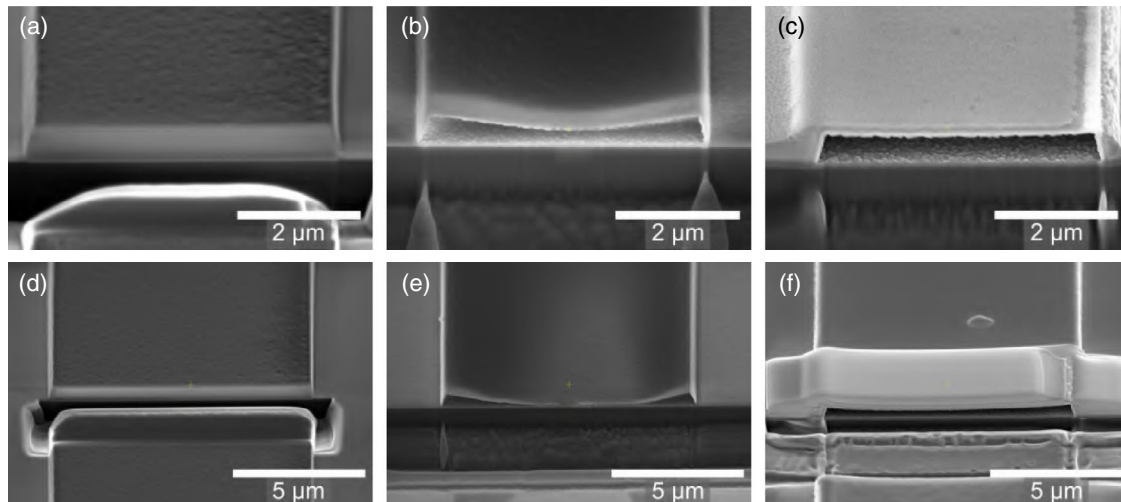
of large-area substrates. Another explanation for this recommendation could be the limited HF mass transport to the etch front. Let us assume that the total mass diffusion length of HF in a gas mixture containing N$_2$ and EtOH is x. The interdiffusion coefficient D'_{HF} of HF vapor in a gas mixture of N$_2$ and EtOH can be found through the Maxwell–Stefan equation.[41,42]

$$D'_{HF} = \frac{1 - Y_{HF}}{Y_{N_2}/D_{HF,N_2} + Y_{EtOH}/D_{HF,EtOH}} \quad (1)$$

where Y_{HF}, Y_{N_2}, and Y_{EtOH} are the molecular fraction of the components. The diffusion coefficient of HF in N$_2$ (D_{HF,N_2}) and HF in EtOH ($D_{HF,EtOH}$) is calculated in Supporting Information (Equation (1)). With this, we obtain an interdiffusion coefficient D'_{HF} of 1.829 cm^2 s^{-1} for HF in the gas composition. A mass diffusion length x of HF in the gas mixture during one etch cycle can then be calculated as

$$x = \sqrt{4D'_{HF}t} \quad (2)$$

where t is the diffusion time. We now set the diffusion time to the cycle time of 400 s that we employed for the most part of our studies. This would result in a diffusion length of 54 cm indicating that the diffusion range of HF in the gas mixture cannot be the limiting factor. Here, we could show that all opening areas, even for as small as 0.6 μm^2 with 600 nm height etch to a depth of close to 500 μm with constant etch rates. This gives reproducible aspect ratios of up to 475:1 etch depth to structure width and up to 507:0.05 (9500:1) etch depth to membrane thickness for a 50 nm Al$_2$O$_3$ membrane. For 20 nm membranes, width to depth ratios of 491:2, and etch depth to membrane thickness ratios of up to 495:0.02 (24750:1) could be achieved. Despite the high diffusion rates, there seems indeed to be a transport limitation for smaller opening areas and a decreased etch rate for smaller structure heights, which we want to further look at.

**ADVANCED
SCIENCE NEWS**

www.advancedsciencenews.com

**ADVANCED
ENGINEERING
MATERIALS**

www.aem-journal.com

Figure 6. Test structures with 600 nm height and 5 and 10 μm width: Cross section of the structure before VHF release step (a,d); Shell membranes after FIB cut (b,e); Shell structures with Pt cover layer after FIB cut (c,f).

experiment and assume that the geometry limits the stability of the shell structure mechanically. In a conservative assumption, the structure can be modeled with linear elasticity assuming that the top membrane is a simply supported beam with uniform load, where the latter is determined by the membrane's own weight (Section S6, Supporting Information). This assumption is conservative as it does not consider the additional support given by the constraint of the etch front and further it does neglect the walls' contribution to the stiffness of the structure. The deformations with this assumption can be therefore considered larger than the ones experimentally observed, if only the structure's weight is considered. The deformation is calculated using the formula as follow

$$\delta_{max} = \frac{5}{32} \frac{\rho g w^4}{E_{Al_2O_3} t^2} \tag{3}$$

where δ_{max} is the deflection at the center of the beam, ρ is the density of ALD Al_2O_3,[43] g is the gravity, w is the width of the beam, $E_{Al_2O_3}$ is the Young's modulus of ALD Al_2O_3,[35] and t is the thickness of the beam. In this case, the maximum deflection would be 8.756×10^{-4} nm (1.401×10^{-4} nm) for a beam with 100 μm width and thickness of 20 nm (50 nm). Considering gravity and mass to be the decisive factors, widths up to 288 μm (455 μm) would be obtainable by keeping the deflection under 600 nm, the height of the shell structure. Obviously, this is in contrast to what was experimentally observed. Structures with 100 μm widths completely collapsed on underlying support independent of the thickness of the membrane (Figure S6, Supporting Information). Even for 10 μm widths, deflections can be observed. Hence, the reason for the observed structural distortions cannot be attributed to the weight of the structure. There could be a chemical change to the Al_2O_3, as it is exposed to HF vapor for prolonged duration with deep under etches. This would entail that the deformation gets larger with the number of etch cycles or with exposure time to the HF etchant. In Figure S4, Supporting Information, we show images of 5,

10, and 100 μm wide shell structures with two different etch depths, 206 μm (SD 6.5 μm) and 494 μm (SD 23 μm) respectively, corresponding to 40 and 99 cycles with recipe R4, respectively. There is a significant change in the optical appearance at the entrance of the structures with 10 μm and particularly with 100 μm width. This corresponds to the deflected zone along the length. The size of this zone seems to correlate with the width but not with the etch depths of the structure. This observation, together with the outstanding etch selectivity of Al_2O_3 for HF vapor in literature,[12] lets us assume that chemical changes are of minor importance. Instead, we hypothesize that intrinsic stress accumulated during the deposition of the Al_2O_3 films on the underlying support, which gets released when etching away the underlying SiO_2. This stress might be accumulated over the entire length of the structure; however, the rigidity of the walls ensures the stability of the top membrane at a certain distance from the opening area. In other words, the limited structural constraint at the opening area might lead to a release of the stress at this location. This coincides with the observation that the deflected zone is strongly width dependent but does not necessarily grow with etch depth. A validation of this hypothesis would entail that a cut through a random location along the length of the structure may release the stress in a similar fashion thereby resulting in a similar deflection. We used FIB to cut out a section of the 50 nm thick and 2, 5, and 10 μm wide shell structures, respectively. The results can be seen in Figure 6 (5 μm width on the left and 10 μm width on the right) and in Figure S4 (2 μm width), Supporting Information. In Figure 6b,e, it can be seen that the FIB cut indeed resulted in a similar deformation of 300 nm (600 nm) for the 5 μm (10 μm) wide structure, respectively. We further constrained the opening area by depositing Pt via the FIB tool before performing the cut in the assumption that this provides extra rigidity to the location and prevents stress release (Figure 6c,f). Indeed, the deformation could be significantly reduced to 0.07 μm (0.2 μm) for the 5 μm (10 μm) wide structure, which further points toward intrinsic stress being the nature of this deformation. As the purpose of this study is

**ADVANCED
SCIENCE NEWS**

www.advancedsciencenews.com

**ADVANCED
ENGINEERING
MATERIALS**

www.aem-journal.com

to show the limits of aspect ratio with ALD and HF vapor processes, it is subject to a further study (in preparation) to investigate the cause of this intrinsic stress. It might however be related to the difference in deposition temperatures of ALD Al_2O_3 (250 °C) and SiO_2 (350 °C),[44] interfacial strain[45] or the film thickness.[35]

2.6. Mechanical Properties of Shell Structures

We envision the applicability of the presented shell structures largely in the MEMS and nanofluidic sector though various types of applications can be leveraged from this type of geometrical control at the nanoscale. As a proof of concept, we investigate the mechanical tunability through geometrical changes of the tunnel-like 3D shell structures. These might be interesting for devices using vibration or resonance as signal. Material properties paired with tunability in geometric shapes can be utilized to tune elasticity, deflection, or contact stiffness beyond a point possible with simple suspended membranes. The opportunities in shapes for tuning structure strength and response are manifold. Our preliminary data in **Figure 7** shows that the structures can be elastically deflected by one fifth of the structure height without leaving optically visible damage to the structure. No deformation fringes were visible in the SEM on the top of the membrane. As expected, the elastic behavior of the structures is dependent on the structure width as well as the membrane thickness. Purely elastic behavior with deflections of 100 and 40 nm for load-controlled measurements with 5 µN assigned load were observed for 50 nm thick shell structures with 10 and 5 µm widths, respectively (Figure 7a). For 20 nm thick shell structures (Figure 7b), the 5 µm width also displayed linear elastic behavior, however with a much lower stiffness and corresponding deflection of 70 nm. As expected, the 20 nm thick and 10 µm wide structure deflected the most. In fact, a load of 1 µN only was sufficient to

deflect the structure by 100 nm. To avoid the problem of not reaching the set point, displacement-controlled measurements were conducted as shown in Figure S9, Supporting Information. We obtained bulk elastic moduli of 112 ± 10.3 and 156.6 ± 6.2 GPa for 20 and 50 nm Al_2O_3 membranes, respectively. The moduli were measured from the unloading curve after compressing the membranes deposited on a Si wafer with 2000 µN (Figure S9, Supporting Information). In comparison, we evaluated the elastic response of the 50 nm thick and released 3D shell structures from the unloading curve during load-controlled experiments (Figure 7a). Equivalent moduli of 252.4 ± 36 and 118.5 ± 0.008 MPa were obtained for structures with 5 and 10 µm shell width, receptively. The structures showed immediate responses and both loading cycles showed a similar trend indicating that the structure remained intact. Remarkably, the modulus of elasticity could be set up to one order of magnitude lower than the bulk modulus. The response of equivalent 20 nm thick 3D shell structures is shown in Figure 7b. An equivalent modulus could not be determined due to the noise in the data. The 5 µm wide membrane showed some nonlinear behavior in the response rendering an assessment of the equivalent modulus difficult. For the 10 µm membrane, the resolution of the experimental setup was insufficient to assess the mechanical properties. For this type of membrane, more characterization is necessary to fully describe its mechanical response. Through our preliminary data on mechanical response of 3D shell structures, we show that the dimensions of the continuous 3D shell structure can be precisely tuned to set the desired mechanical response. Though we are not limiting the applicability of such structures to MEMS sensors, we assume that such a structure coated with a conformal thermo-sensing coating may serve as a high-precision tunable bolometer with a high signal-to-noise ratio.

To summarize, we could show the successful release of ALD Al_2O_3 shell structures with 20 and 50 nm wall thickness with
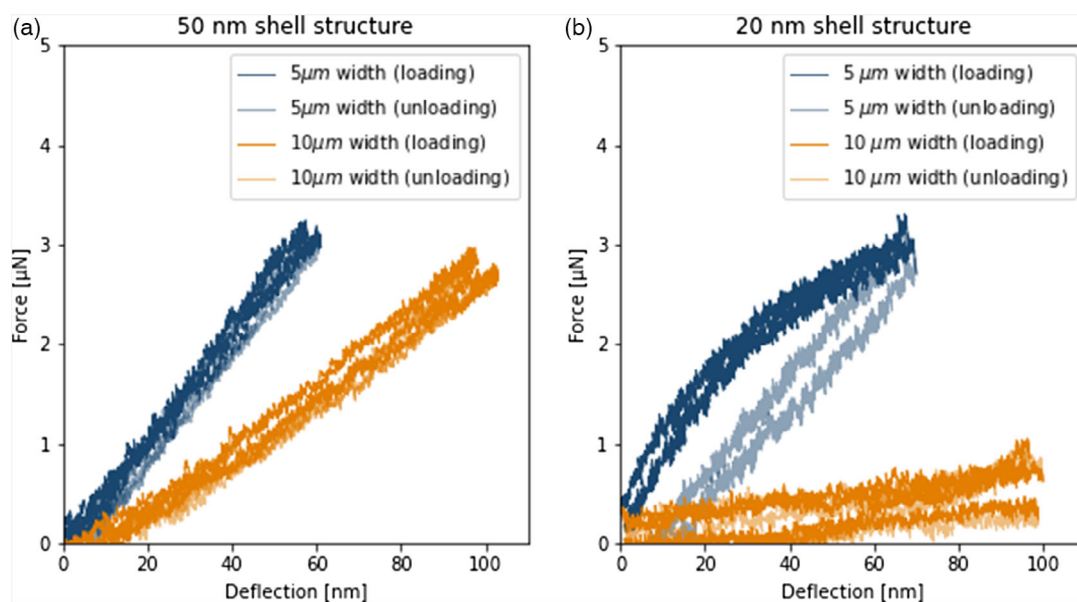

Figure 7. Nanoindentation measurements on ALD Al_2O_3 shell structures with width of 5 and 10 µm: a) Load-deflection signal for 50 nm shell structure width and b) Load deflection signal for 20 nm thick shell structure.

opening areas of 0.6, 1.2, 3, 6, and 60 μm² (0.2, 0.5, 1, and 10 μm²) widths with 0.6 μm (0.1 μm) height. All geometries were etched to a total depth of 0.5 mm providing remarkable aspect ratios of 9500:1 etch depth to membrane thickness and 475:1 etch depth to width for wall thicknesses of 50 nm Al_2O_3. There are limitations to both the width of the opening area and the predictable etch depth. Concerning the latter, etch rates decrease with longer etch times and smaller opening areas. Generally, etch rates are slightly lower for structures with lower height, while particularly smaller widths (2 and 5 μm) resulted in a stagnation of the etch depth at total etch times above 600 min. Structures with larger widths (5 μm and above) significantly deform at the opening area, where the deformation seems independent of the exposure time to the etchant. We relate this deformation to intrinsic stress accumulated during the deposition of the Al_2O_3 films. Due to the freedom in design with the presented approach, the elasticity of such structures can be precisely tuned changing the width and thickness. For 50 nm thick 3D shell structures, the equivalent elastic modulus could be reduced by one order of magnitude with respect to the bulk modulus of ALD Al_2O_3. The elasticity of the 20 nm is expectedly even smaller. However, we were unable to assess it with our experimental procedure. It can however be said that all structures remained intact after mechanical loading.

3. Conclusion

In the context of generating high aspect ratio deep-etched shell structures of ALD Al_2O_3 with a continuous etching process, we explore the limits of vapor HF technology at the very edge of its possibilities. Using ALD Al_2O_3 etch-stop layers and HF vapor release processes, the fabrication of self-supporting membrane shell structures with wall thickness of 20 and 50 nm and undercut depth over 500 μm in longitudinal direction without additional etch holes was achieved. This resulted in aspect ratios as high as 24 750:1 etch depth to membrane thickness for a 20 nm thick Al_2O_3 membrane structure and 475:1 etch depth to width for wall thicknesses of 50 nm Al_2O_3, which can be attributed to the high selectivity of Al_2O_3 over the sacrificial SiO_2 material. The vapor etch process contained HF, EtOH, and N_2, where the etch rate increased with HF share but stagnated at a gas composition of 31.4% HF. To achieve deep etches with reproducible rates of 0.75 nm min^{-1}, 400 s cycle time rendered a good reproducibility. The depth follows a linear relationship with the total etch time, which seems relatively independent from the width of the structure for the investigated geometries with 600 nm height. Reducing the height to 100 nm, however, reduced the rates as the etch depth increased and led to a stagnation for smaller widths ≤ 0.5 μm². Structural distortions can only be observed at the opening area, where widths ≥ 10 μm deformed, initially only slightly until their complete collapse at 100 μm width. Our findings show that this can be related to the internal stress of the membrane built up during the deposition process. In preliminary mechanical assessment studies through nanoindentation, we further show that the structures can be precisely controlled in their mechanical response, where the equivalent elastic modulus of the structure could be reduced by up to one order of magnitude for 50 nm thick structures compared to the bulk thin film. All investigated structures remained intact after loading. This work explores the limits of aspect ratios of free-standing shell structures and will serve future researchers as a guideline for gaining performance out of extreme geometries.

4. Experimental Section

Test Structure Fabrication: Test structures, in the form of shell structures (Figure 1), were fabricated to assess the etch-stop quality and the release limitations within the HF-etching process. These structures were fabricated as shown in **Figure 8**a–e and Figure S2, Supporting Information. The substrate material was a < 100 > Si wafer, resistivity 5–10 ohm cm
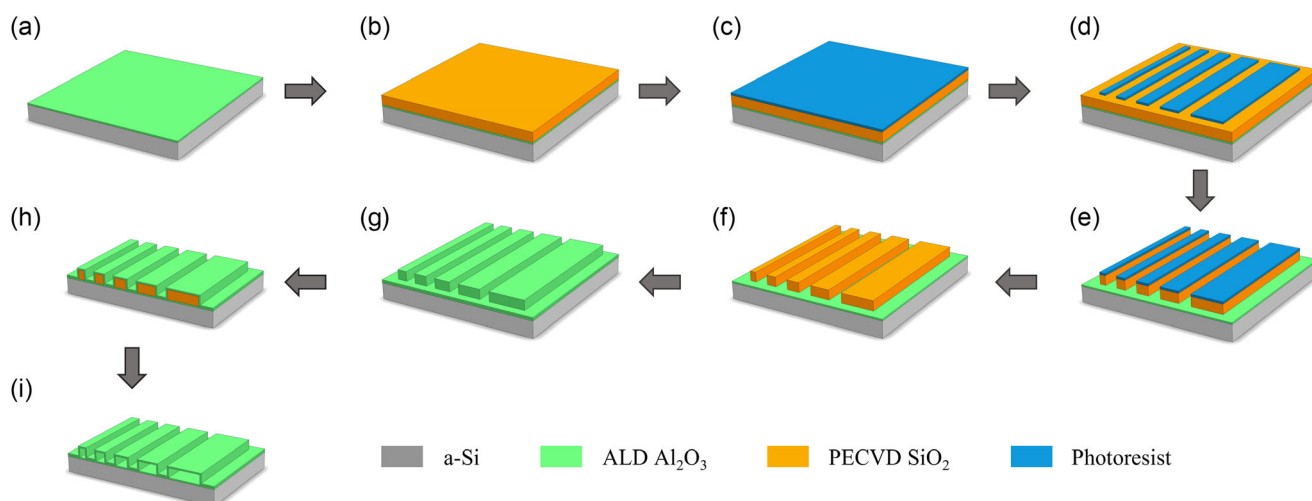

Figure 8. Schematic of the process flow: a) t-ALD Al_2O_3 etch-stop layer deposited onto cleaned Si wafer; b) Sacrificial PECVD SiO_2 layer deposited onto Al_2O_3 etch-stop layer c) Spin-coating of photoresist; d) Lithographic structuring of photoresist; e) Removal of sacrificial SiO_2 in a dry etch process; f) Removal of remaining photoresist in a solvent clean process; g) Enclosing sacrificial SiO_2 structures with an ALD Al_2O_3 etch-stop layer; h) Cleaving of structure orthogonally to the pattern to facilitate gas access; i) VHF etching of sacrificial SiO_2.

(WaferPro, Santa Clara, California, USA), that underwent an Radio Corporation of America cleaning procedure. In the first step (a), Al_2O_3 was deposited at 250 °C in a thermal atomic layer deposition (t-ALD) system (Savannah, Cambridge, USA) using trimethylaluminum (TMA, Sigma-Aldrich, USA) and deionized water (H_2O) as precursors. Deposition was done with a carrier gas flow of 20 sccm, pulse time of 0.015 s, and wait time of 12 s. The 20 and 50 nm films were deposited, respectively. In a second step (b), a sacrificial SiO_2 layer was deposited onto the Al_2O_3 using PECVD (Shuttlelock PECVD, Plasma-Therm, USA). Chamber pressure was set to 1100 mTorr with substrate temperature of 300 °C. A gas flow of 250 sccm silane (SiH_4), 1700 sccm dinitrogen oxide (N_2O), and 800 sccm helium (He) were applied. Thicknesses of 100, 300, and 600 nm were deposited, respectively, to define the height of the resulting shell structures. Parallel SiO_2 line patterns of different cross-sectional dimensions were then fabricated in a lithography step. For this, positive-tone photoresist (Shipley 3612, Dow, USA) was spun on the SiO_2 layer (1 μm) (c) and patterned using an exposure dose of 100 mJ cm^{-2} (d) in a maskless aligner (MLA) 150 (Heidelberg Instruments Mikrotechnik, Heidelberg, Germany). Then, the exposed resist was developed in a standardized process for 1 min on an automated track system (Silicon Valley Group, USA) with MF-26 A as developer. An ICP-RIE dry etch process (e) (Versaline ICP, Plasma-Therm, USA) was employed to etch the exposed SiO_2 regions down to the etch-stop layer. Etch gas composition with 2 sccm oxygen (O_2) and 45 sccm trifluoromethane (CHF_3) were applied. In a solvent-cleaning step, the substrate was immersed in acetone, isopropanol, and ethanol to remove the remaining photoresist (f). Then (g), another t-ALD Al_2O_3 etch-stop layer was deposited as in (a) resulting in shell structures of constant wall thickness. The thickness of the Al_2O_3 layers was measured by spectroscopic ellipsometry after step (a) and (g), confirming the layer thickness was 20 and 50 nm and 40 and 100 nm after step (a) and (g), respectively. To provide openings for the etch gas to access the sacrificial material, the shell structures were cleaved orthogonally to their lengths leaving specimens with 2 mm × 5 mm dimensions (h) containing various shell structure widths with constant heights. In a VHF etch process, the shell structure was released by etching the sacrificial SiO_2 in a Primaxx uetch tool (SPTS, Newport, UK) (i). VHF etching was done at 45 °C and 125 Torr pressure with varying gas compositions and cycle times. The exact gas composition of all employed recipes is shown in Table 1, where the share of nitrogen (N_2), ethanol (C_2H_5OH), and HF is displayed. The gas composition for each recipe was based on the recommendation of SPTS with HF flow rate between 100 and 720 sccm, while the total flow rate was kept below 1925 sccm. The cycle time employed in this study varied between 240 and 600 s and the total etch time was up to 11 h.

Mechanical Characterization: Deformation analysis of the free-standing shell structures without applied load was done using FIB, where cross section were cut prior to release and after release of the shell membranes. A large multistep cross section was made before a cleaning cross-section milling was applied with ion beam settings of 30 kV acceleration voltage and 90 pA beam current. To compare the shell structure profile in various conditions, we coated the shell structures with ion-beam-induced deposition platinum prior to cross sectioning.

Mechanical properties of the Al_2O_3 thin film and measurements of the elastic moduli of the bulk thin films deposited on the substrate were done using nanoindentation. The measurements were conducted at room temperature using a commercial nanoindenter TI-950 from Hysitron (Blue Scientific, Cambridge, UK) with a nanoDMX Transducer head, equipped with a standard Berkovich tip. The tip was provided by Synton-MDP (Nidau, Switzerland). Indentation was performed at a maximum indentation depth of 70% of the film thickness to limit the influence of the substrate. After an initial drift correction, the indentation procedure followed a trapezoidal profile with a loading segment at constant strain rate for 5 s, a holding segment of 2 s at the maximum load, and an unloading segment at constant strain for 5 s. Representative load curves and the indentation measurements for samples with 20 and 50 nm shell thickness are shown in Figure S9, Supporting Information.[46] Prior to indentation, the tip was calibrated against the elastic modulus of fused silica. The elastic modulus was calculated from the reduced elastic modulus E_r (GPa) using Equation (4)[35]

$$\frac{1}{E_r} = \frac{(1 - \nu_f^2)}{E_f} + \frac{(1 - \nu_i^2)}{E_i} \tag{4}$$

where the subscript f refers to the film and the subscript i refers to the indenter tip. The elastic modulus E_i and poisson's ratio ν_i of the indenter tip are assumed to be 1141 and 0.07 GPa, respectively.[47,48]

Mechanical response of 3D shell structures point deflection measurements were carried on the shell structures with width of 5 and 10 μm, respectively, employing the same instrument using the same indenter tip as the bulk property measurement (Section 4.2a). To avoid punching trough the membrane or causing permanent deformation, indentation loads below 10 μN were used. Both load-controlled and displacement-controlled measurements were conducted. Once the tip engaged the sample surface, the instrument was capable of resolving load increments of 1 nN force and displacement resolution of 0.04 nm along the indentation axis according to manufacturer data. Loads between 3 and 30 μN and displacement-controlled measurements with displacements up to 200 nm (Figure S10, Supporting Information) were studied. Indentation was done on shell structures with 20 and 50 nm shell thickness and 5 and 10 μm width, respectively. The indenter tip was placed midway between the sidewalls on the top membrane. To exclude areas with initial deformation on the entrance section of the 3D shell structures, a sufficient distance to the opening area was kept. The optical imaging possibilities in the system were used to define indentation points in the center of the shell structure geometry.

Supporting Information

Supporting Information is available from the Wiley Online Library or from the author.

Conflict of Interest

The authors declare no conflict of interest.

Data Availability Statement

The data that support the findings of this study are available from the corresponding author upon reasonable request.

[1] L. Goossen, J. Wei, G. Pandraud, V. Prodanovic, P. M. Sarro, *Proceedings* **2018**, *2*, 13.

[2] S. Mehraeen, J. T. McKeown, P. V. Deshmukh, J. E. Evans, P. Abellan, P. Xu, B. W. Reed, M. L. Taheri, P. E. Fischione, N. D. Browning, *Microsc. Microanal.* **2013**, *19*, 2.

[3] L. F. Allard, S. H. Overbury, W. C. Bigelow, M. B. Katz, D. P. Nackashi, J. Damiano, *Microsc. Microanal* **2012**, *18*, 656.

[4] S. An, N. K. Gupta, Y. B. Gianchandani, *J. Vac. Sci. Technol. A* **2013**, *32*, 01A101.

[5] M. Esashi, in *Packaging, Sealing, and Interconnection*, John Wiley & Sons, Hoboken, NJ **2021**, pp. 377–407, Chapter 17.

[6] M. Winterkorn, A. Dadlani, Y. Kim, J. Provine, F. Prinz, in *2015 Transducers – 2015 18th Inter. Conf. on Solid-State Sensors, Actuators and Microsystems*, Tranducers **2015**, pp. 2272–2275.

[7] H. Ritala, J. Kiihamäki, M. Heikkilä, *Microelectron. Eng.* **2010**, *87*, 501.

[8] T. Zhu, P. Argyrakis, E. Mastropaolo, K. K. Lee, R. Cheung, *J. Vac. Sci. Technol., B: Microelectron.* **2007**, *25*, 2553.

[9] A. Witvrouw, B. Bois, P. De Moor, A. Verbist, C. Van Hoof, H. Bender, C. Baert, *Proc. SPIE—Int. Soc. Opt. Eng.* **2000**, 4174.

[10] J. Valle, D. Fernández, J. Madrenas, *J. Microelectromech. Syst.* **2016**, *25*, 401.

[11] T. S. English, J. Provine, A. F. Marshall, A. L. Koh, T. W. Kenny, *Ultramicroscopy* **2016**, *166*, 39.

[12] M. M. Winterkorn, H. J. Kim, J. Provine, in *Etch Rate Characterization of Oxide ALD Films*, AVS **2019**, https://www.avssymposium.org/ALD2019/Sessions/SupplementalDocumentDownload/36487?sessionId=36510.

[13] J. Bühler, F.-P. Steiner, H. Baltes, *J. Micromech. Microeng.* **1997**, *7*, 1.

[14] M. Ghaderi, N. P. Ayerden, G. de Graaf, R. F. Wolffenbuttel, *Proc. Eng.* **2015**, *120*, 816.

[15] J. Philippe, I. Ouerghi, O. Pollet, S. Hentz, J. Arcamone, T. Ernst, *ECS Trans.* **2014**, *61*, 395.

[16] H. Saloniemi, M. Tuohiniemi, *Solid State Phenom.* **2012**, *187*, 45.

[17] H. Ni, H.-J. Lee, A. G. Ramirez, *Sens. Actuator A Phys.* **2005**, *119*, 553.

[18] A. Shafikov, B. Schurink, R. van de Kruijs, J. Benschop, W. van den Beld, Z. Houweling, F. Bijkerk, *Sens. Actuator A Phys.* **2021**, *317*, 112456.

[19] M. Berdova, in *Micromechanical Characterization of ALD Thin Films*, Thesis, Aalto University, **2015**.

[20] A. A. Dedkova, P. Y. Glagolev, G. D. Demin, E. E. Gusev, P. A. Skvortsov, in *IEEE Conf. of Russian Young Researchers in Electrical and Electronic Engineering (EIConRus)*, IEEE, Piscataway, NJ **2020**, pp. 2288–2292.

[21] M. Sterner, G. Stemme, J. Oberhammer, in *IEEE 5th Inter. Conf. on Nano/Micro Engineered and Molecular Systems*, IEEE, Piscataway, NJ **2010**, pp. 959–962.

[22] R. Liu, B. Jiao, Y. Kong, Z. Li, H. Shang, D. Lu, C. Gao, D. Chen, *J. Micromech. Microeng* **2013**, *23*, 095019.

[23] J. Yang, C. Peters, O. Paul, in *Transducers '01 Eurosensors XV.* Springer Berlin Heidelberg, Berlin, Heidelberg, **2001**, pp. 1366–1369.

[24] S. Yoneoka, M. Liger, G. Yama, R. Schuster, F. Purkl, J. Provine, F. B. Prinz, R. T. Howe, T. W. Kenny, in *IEEE 24th Inter. Conf. on Micro Electro Mechanical Systems*, IEEE, Piscataway, NJ **2011**, pp. 676–679.

[25] W. I. Jang, C. A. Choi, M. L. Lee, C. H. Jun, Y. T. Kim, *J. Micromech. Microeng.* **2002**, *12*, 297.

[26] J. Anguita, F. Briones, *Sens. Actuator A Phys.* **1998**, *64*, 247.

[27] A. A. P. Kshirsagar, A. S. S. Malani, E. V. S. Tiware, *Int. J. Eng.* **2017**, *10*, 162.

[28] J. Xu, Y. Zhang, Q. Yu, L. Zhang, *Thin-Wall. Struct.* **2022**, *170*, 108619.

[29] A. Lakhtakia, R. J. Martn-Palma, in *Engineered Biomimicry*, Newnes, London, UK **2013**.

[30] P. Du, W. Wei, D. Liu, H. Kang, P. Liu, *Chem. Eng. J.* **2018**, *335*, 373.

[31] V. N. Popov, *Mater. Sci. Eng. R Rep.* **2004**, *43*, 61.

[32] A. Lahiri, A. Willert, S. Z. E. Abedin, F. Endres, *Electrochim. Acta* **2014**, *121*, 154.

[33] H. E. Lim, Y. Miyata, R. Kitaura, Y. Nishimura, Y. Nishimoto, S. Irle, J. H. Warner, H. Kataura, H. Shinohara, *Nat. Commun.* **2013**, *4*, 1.

[34] A. Kumar, Ashudeep, D. Bansal, P. Kumar, Anuroop, Khushbu, K. Rangra, *Microelectron. Eng.* **2020**, *221*, 111192.

[35] M. K. Tripp, C. Stampfer, D. C. Miller, T. Helbling, C. F. Herrmann, C. Hierold, K. Gall, S. M. George, V. M. Bright, *Sens. Actuator A Phys.* **2006**, *130–131*, 419.

[36] T. Bakke, J. Schmidt, M. Friedrichs, B. Völker, *Micromech. Eur.* **2005**, *122*, 68.

[37] E. H. Cook, M. J. Tomaino-Iannucci, D. P. Reilly, M. G. Bancu, P. R. Lomberg, J. A. Danis, R. D. Elliott, J. S. Ung, J. J. Bernstein, M. S. Weinberg, et al., *J. Microelectromech. Syst.* **2018**, *27*, 1071.

[38] D. Vestyck, *Product Manager At SPTS Technologies Ltd.*, Personal Communication, **2022**.

[39] *"uEtchHF VaporRelease System"*, Equipment Manual, Marvell Nanofabrication Laboratory, UC Berkely, https://nanolab.berkeley.edu/public/manuals/equipment_manual.shtml (accessed: April 2022).

[40] SPTS Technologies, *Uetch Primaxx System Manual*, **2012**.

[41] T. K. Thomas K. Sherwood, R. L. Pigford, C. R. Wilke, *AIChE J.* **1976**, *22*, 620.

[42] J. O. Hirschfelder, C. F. Curtiss, R. B. Bird, *J. Polym. Sci.* **1955**, *17*, 116.

[43] M. Groner, F. Fabreguette, J. Elam, S. George, *Chem. Mater.* **2004**, *16*, 639.

[44] O. M. E. Ylivaara, X. Liu, L. Kilpi, J. Lyytinen, D. Schneider, M. Laitinen, J. Julin, S. Ali, S. Sintonen, M. Berdova, E. Haimi, T. Sajavaara, H. Ronkainen, H. Lipsanen, J. Koskinen, S.-P. Hannula, R. L. Puurunen, *Thin Solid Films* **2014**, *552*, 124.

[45] F. Spaepen, *Acta Mater.* **2000**, *48*, 31.

[46] A. C. Fischer-Cripps, in *Nanoindentation*, Springer, New York **2002**, pp. 159–173.

[47] J. Proost, F. Spaepen, *J. Appl. Phys.* **2002**, *91*, 204.

[48] J. Beuth Jr., *Int. J. Solids Struct.* **1992**, *29*, 1657.